ScieRxiv

NOT PEER-REVIEWED

Research Article

Synergistic structural coupling of MXene and La-Ti-O MOF for high-energy-density flexible solid-state supercapacitors

Haiqing Hu, Ping Cai*, Xinjie Lv, Yaoben Xu, Yating Du, Kexiang Zhang, Songwei Wang*, Huanzhi Zhang, Fen Xu, Lixian Sun*

Guangxi Key Laboratory of Information Materials, Guangxi Collaborative Innovation Center for Structure and Properties for New Energy and Materials, School of Materials Science and Engineering, Guilin University of Electronic Technology, Guilin 541004, Guangxi, China.

***Correspondence to:** Prof. Ping Cai, Prof. Songwei Wang, Prof. Lixian Sun, Guangxi Key Laboratory of Information Materials, Guangxi Collaborative Innovation Center for Structure and Properties for New Energy and Materials, School of Materials Science and Engineering, Guilin University of Electronic Technology, Guilin 541004, Guangxi, China. Email: caiping@guet.edu.cn; swwang@guet.edu.cn; sunlx@guet.edu.cn

Received: 27 May 2026 | Approved: 05 June 2026 | Online: 05 June 2026

Abstract

For energy storage applications, the practical potential of single materials is usually limited by their intrinsic drawbacks. Specifically, metal-organic frameworks (MOFs) suffer from poor conductivity, while 2D MXenes are prone to oxidation and restacking. Herein, in situ growth of La-Ti-O MOF on $Ti_3C_2T_x$ MXene is reported to enable

synergistic structural coupling of MXene@La-Ti-O composite for high-performance supercapacitors. La-Ti-O MOF is *in-situ* grown from lanthanum-coordinated titanium-oxo cluster precursors on MXene nanosheets, and the synergistic structural coupling of MXene@La-Ti-O can effectively inhibit the restacking of MXene nanosheets, enrich redox active sites, and simultaneously enhance the oxidation resistance and mechanical toughness of free-standing film. The MXene@La-Ti-O film electrode shows excellent electrochemical performance with high capacitance of 663 F g^{-1} at 1 A g^{-1} and high stability of 96% retention after 20,000 cycles. Moreover, the MXene@La-Ti-O symmetric supercapacitor exhibits superior energy storage performance with energy density of 58.93 Wh kg^{-1} at power density of 400 W kg^{-1}, which is among the best performances reported so far for MXene-based flexible symmetric solid-state supercapacitors. The impressive results indicate the synergistic structural coupling strategy of MXene and La-Ti-O MOF is very promising for high-performance flexible supercapacitors.

Keywords: $Ti_3C_2T_X$ MXene, metal-organic frameworks (MOFs), titanium-oxo cluster, flexible supercapacitors, energy storage performance

INTRODUCTION

With the rapid advancement of flexible electronics and the growing demand for distributed and portable energy solutions, flexible energy storage systems have garnered considerable attention due to their superior compatibility and mechanical adaptability[1-4]. As next-generation energy storage devices, flexible supercapacitors have emerged as highly promising candidates for portable and wearable electronics, owing to their outstanding mechanical flexibility, excellent electrochemical performance, high safety, and seamless integration capabilities[5,6]. In recent years, the design and fabrication of advanced functional materials for energy storage and conversion have become a focal area of academic research, and remarkable progress has

been achieved with a variety of functional materials, including MXenes, metal-organic frameworks (MOFs), covalent organic frameworks (COFs), and other nanomaterials[7-9]. MXenes are two-dimensional (2D) transition metal carbides or nitrides with a general formula of $M_{n+1}X_nT_x$, where M represents early transition metals (e.g. Ti, V, Nb, Mo, Zr, Hf), A denotes a Group III or IV element (e.g. Al, Si, Ga), X refers to carbon or nitrogen, and T_x signifies surface functional groups (e.g. =O, -F, -OH, -Cl)[10,11]. MXenes exhibit metallic-like electrical conductivity, a unique layered structure, abundant surface functional groups, and excellent solution processability, making them highly attractive for energy storage and conversion applications, flexible sensors, and *etc.*[12-14]. MOFs, a class of crystalline porous materials constructed by coordinating metal ions or clusters with organic ligands, feature well-defined nanochannels and cavities with highly tunable structures[10,15-19]. Distinguished by their ultrahigh specific surface areas and precisely controllable pore sizes, MOFs have been widely recognized as promising functional materials in electrochemical energy storage and conversion fields. However, the practical application of single-component materials is often constrained by their intrinsic limitations. For instance, MOFs generally suffer from inadequate electrical conductivity, while MXenes prepared through etching reactions inevitably expose a large number of unsaturated metal atoms on their surfaces, leading to susceptibility to oxidation and insufficient cycling stability[20]. In addition, MXene nanosheets are prone to re-stacking due to the inner strong interaction, which results in the aggregation/precipitation of nanosheets, and thus severely restrict the ions transport and electrochemical performance of MXene film[21,22].

To address these limitations, researchers have developed various strategies, such as integrating MOFs with highly conductive materials, and combining MXenes with structurally robust components. For instance, organic molecules (e.g. tannic acid) and carbon nanomaterials were used to modify the surface of MXenes, and thus enhance the oxidation resistance and interlayer spacing[23-25]. Recently, constructing MOF/MXene

composites has proven to be an effective approach to achieving enhanced overall performance[26]. Wu and colleagues developed a method using V_2CT_x MXene as a metal source to synthesize MOF nanosheets, and the resulting V_2CT_x-PMOF composite demonstrated excellent proton conductivity[27,28]. Zheng *et al.* proposed a simple yet effective hybridization strategy for synthesizing MXene@Ni-MOF composites by integrating Ti_3C_2 MXene with 3D columnar porous MOF nanosheets, where the synergistic interactions between MXene and Ni-MOF substantially enhanced the specific capacitance[29]. Compared with conventional MXene-based composite systems (e.g., MXene/organic or MXene/carbon composites), MXene/MOF composites offer greater structural flexibility for supercapacitor electrode applications[30,31]. Nevertheless, synthesizing novel MXene/MOF composites that simultaneously possess high oxidation resistance, excellent electrochemical performance, and mechanical flexibility remains a critical challenge.

Titanium-oxygen (Ti-O) clusters are discrete, multinuclear metal-oxygen clusters constructed through covalent or coordination bonding between titanium ions and oxygen-containing ligands such as hydroxyl (-OH) and oxo (=O) groups, and atomic-level precise regulation of cluster core size and ligand structure can be achieved by controlling the titanium source, ligand types, and reaction conditions[32,33]. In this work, we propose a strategy that employs $Ti_3C_2T_x$ MXene nanosheets as a substrate to assist the *in-situ* growth of a La-Ti-O MOF structure via the coordination of lanthanum metal ions with titanium-oxygen cluster precursors, and thus synthesize the MXene@La-Ti-O composite. The *in-situ* grown La-Ti-O MOF effectively inhibits the restacking of MXene nanosheets and modulates the pore structure of the composite, thereby optimizing the ion diffusion pathways and increasing the redox active sites. Simultaneously, the structural coupling of MXene@La-Ti-O improves the oxidation resistance and mechanical toughness of free-standing film. The MXene@La-Ti-O film electrode shows excellent electrochemical performance with high capacitance of 663 F

g^{-1} at 1 A g^{-1} and high stability of 96% retention after 20,000 cycles. Moreover, the MXene@La-Ti-O symmetric supercapacitor exhibits superior energy storage performance with energy density of 58.93 Wh kg^{-1} at power density of 400 W kg^{-1}, and possesses excellent cycling stability with a high capacitance retention of 84% after 5000 cycles at 10 A g^{-1}. In addition, the MXene@La-Ti-O devices show similar GCD curves under bending angles of 0°, 45°, and 90°, and the brightness of the LEDs remains almost unchanged under bending condition, indicating high bending stability.

EXPERIMENTAL

Materials

MAX (Ti_3AlC_2, 400 mesh) was purchased from Jilin 11 Technology Co., Ltd. The other chemicals were purchased from Shanghai Aladdin Biochemical Technology Co., Ltd.

Preparations

Preparation of $Ti_3C_2T_x$ MXene

According to the previous reports[25,26], single/few-layer $Ti_3C_2T_x$ MXene was synthesized by using HCl/HF etchant to etch Al atoms of Ti_3AlC_2 phase and then using LiCl intercalant for the delamination. Filter a certain amount of colloidal solution through a hybrid cellulose membrane and measure the concentration of the $Ti_3C_2T_x$ dispersion (~10 mg mL^{-1}).

Preparation of MXene@La-Ti-O thin film electrode

Add $Ti(OiPr)_4$(0.61mL, 2mmol), benzoic acid (1.22 g, 10 mmol), an aqueous solution of lanthanum chloride (lanthanum ions 80mg, 0.2 mmol), and 20 mg of $Ti_3C_2T_x$ MXene colloidal solution into 6 mL of CH_3CN. Stir the mixture for 30 min, then transfer it into a high-pressure reactor and protect it with inert nitrogen gas. Heat it in an oven at 100 °C for 72 h. After cooling to room temperature, centrifuge and wash multiple times to replace the organic solvent with an aqueous solvent. Dry the resulting powder in a

vacuum drying oven for the next step. Disperse different amounts of the above powder in deionized water by ultrasonication, add $Ti_3C_2T_x$ MXene, and stir the mixture for 6 h. Then vacuum filter and dry under vacuum at 50 °C for 4 h to obtain self-supporting MXene@La-Ti-O film electrodes with different loading amounts.

Preparation of flexible symmetric sandwich supercapacitor devices

The standalone MXene@La-Ti-O film electrode was cut to 1.5 × 2.5 cm^2, and the PVA/H_2SO_4 solid gel electrolyte was cut to 1.8 × 2.8 cm^2 to serve as the separator. The separator was soaked in 1 M dilute sulfuric acid on both sides, then the MXene@La-Ti-O film electrodes were symmetrically attached to both sides of the separator. Next, copper conductive tapes were symmetrically attached to the surfaces of the two electrodes. Finally, the flexible symmetric supercapacitor device was simply encapsulated using a PET substrate.

Characterizations

Electrochemical measurement

The electrochemical performance of $Ti_3C_2T_x$ and MXene@La-Ti-O film electrodes was measured using a three-electrode system, where the film electrode served as the working electrode, carbon cloth as the counter electrode, Ag/AgCl as the reference electrode, and 3M H_2SO_4 as the electrolyte. Electrochemical measurements of the film electrodes and supercapacitor devices (CV, GCD, and EIS) were conducted at room temperature using a CHI 760E electrochemical workstation.

Calculation

Specific capacitances were calculated by the following equations: $C_g=\frac{(I\,\Delta t)}{(m\,\Delta V)}$, $C_g=\frac{A}{2mv}\Delta V$, $C_a=\frac{A}{2Sv}\Delta V$, where C_g is the gravimetric capacitance, I is the current density (A g^{-1}), Δt represents the discharge time (s), m is the mass of working electrode (g), and ΔV is the potential window (V), A is the integral area of the CV curve, C_a is the areal

capacitance (mF cm^{-2}), v is the scan rate (V s^{-1}), S is the area of electrode (cm^2). The energy density (E_g, Wh kg^{-1}), power density (P_g, W kg^{-1}), areal energy density (E_a, μWh cm^{-2}) and areal power density (P_a, μW cm^{-2}) were calculated according to the following equations: $E_g = \frac{1}{2} C_g (\Delta V)^2 / 3.6$, $P_g = 3600\, E_g / \Delta t$, $E_a = \frac{1}{2} C_a (\Delta V)^2 / 3.6$, $P_a = 3600\, E_a / \Delta t$.

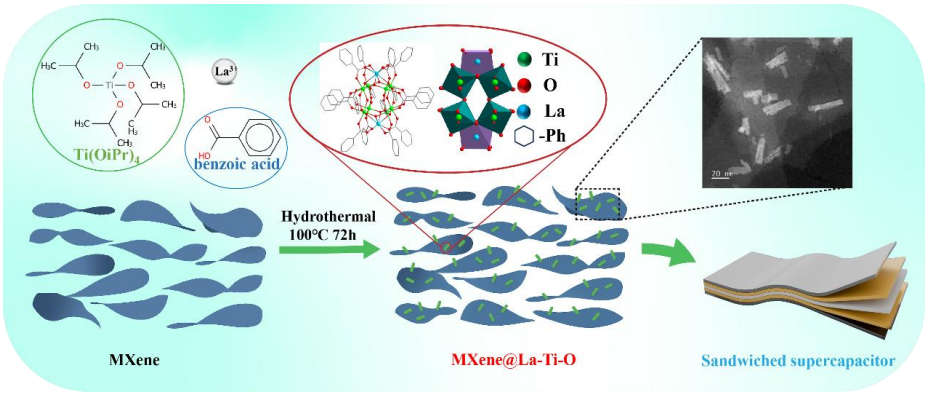

Figure 1. Schematic illustration about the preparation of MXene@La-Ti-O composite, where the internal TEM image shows the rod-shaped La-Ti-O MOF in situ grown on MXene.

RESULTS AND DISCUSSION

Preparation and characterization of MXene@La-Ti-O

According to our previous reports[25,26], the Al atoms in the precursor (Ti_3AlC_2 MAX) were selectively etched using a mixed etchant of hydrofluoric acid and hydrochloric acid (HCl:HF), then followed by intercalation with LiCl to obtain the pristine $Ti_3C_2T_x$ MXene solution. As shown in Figure 1, the precursor for MOF growth, consisting of $Ti(OiPr)_4$, benzoic acid, and an aqueous solution of lanthanum chloride, was mixed with the pristine $Ti_3C_2T_x$ MXene solution, and then subjected to a protective hydrothermal treatment of 100 °C and 72 h to prepare a composite of La ion coordinated titanium-oxygen clusters in situ grown on MXene, denoted as MXene@La-Ti-O. The internal TEM image in Figure 1 shows the rod-shaped La-Ti-O MOF in situ grown on MXene, forming the composite of MXene@La-Ti-O. In order to highlight and analyze

the XRD pattern of La-Ti-O MOF cluster, a pure La-Ti-O sample and a MXene@La-Ti-O sample with 2% MXene (mass content) were prepared for comparison. As shown in Figure 2A, the MXene@La-Ti-O sample with 2% MXene shows a typical (002) peak of MXene, and exhibits similar peaks with the La-Ti-O sample. In addition, the XRD patterns of La-Ti-O MOF for both the MXene@La-Ti-O sample and the La-Ti-O sample are consistent with the previous report[34], indicating the successful preparation of La ion coordinated titanium-oxygen clusters in situ grown on MXene (MXene@La-Ti-O). Unless otherwise specified below, the MXene content and the La-Ti-O cluster content in MXene@La-Ti-O composite are 77% and 23%, respectively.

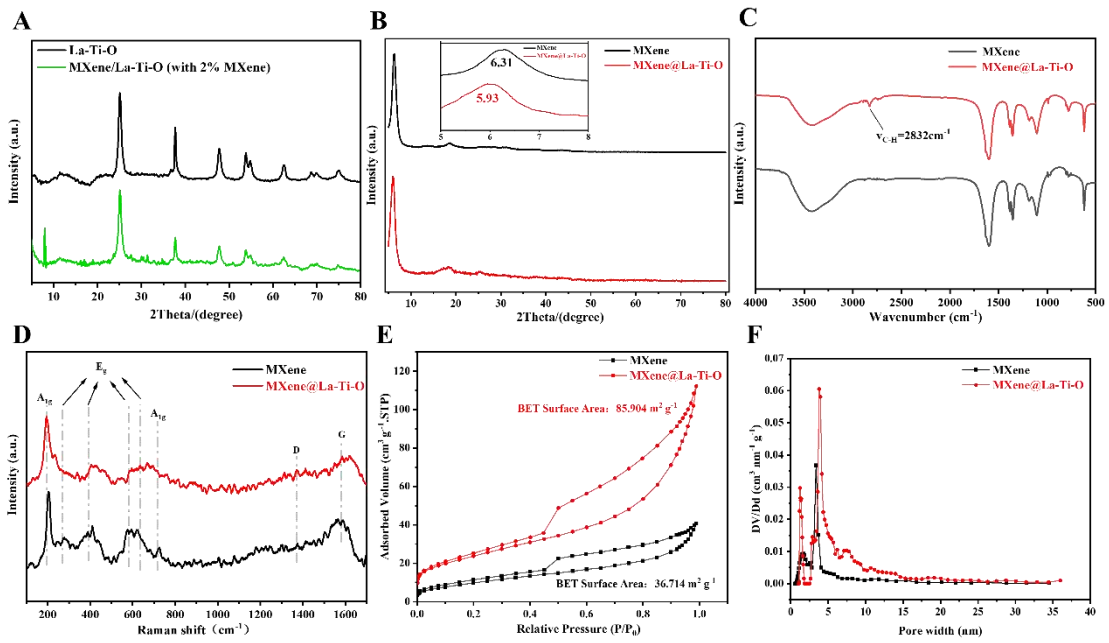

Figure 2. (A) XRD patterns of La-Ti-O MOF and MXene@La-Ti-O (with 2% MXene); (B) XRD patterns; (C) Infrared spectra; (D) Raman spectra; (E) BET adsorption curves and specific surface area data; and (F) pore size distribution curves for MXene and MXene@La-Ti-O.

Figure 2B displays the XRD patterns of MXene and MXene@La-Ti-O. Compared with the (002) peak of the pristine MXene at 6.31°, the (002) peak of MXene@La-Ti-O

appears at a smaller angle of 5.93°, indicating that the *in-situ* grown La-Ti-O MOFs increase the lattice spacing of MXene. As shown in Figure 2C, the Infrared spectrum of MXene@La-Ti-O shows an extra peak at 2,832 cm^{-1} compared to MXene, which corresponds to the vibration peak of C−H in the benzene ring from La-Ti-O MOF[35,36]. Figure 2D displays the Raman spectra of MXene and MXene@La-Ti-O. The peaks around 206 and 725 cm^{-1} correspond to the characteristic A_{1g} out-of-plane symmetric vibrations of Ti and C atoms, while the E_g group vibrations, representing in-plane modes involving Ti, C, and surface termination atoms, appear near peaks at 270, 388, 576, and 635 cm^{-1}[24,25,37]. Compared with pristine MXene, MXene@La-Ti-O shows relatively decreased A_{1g} and E_g characteristic peaks, indicating that the coupling between MXene nanosheets is weakened after the introduction of La-Ti-O, which can effectively alleviate the restacking of MXene nanosheets. The peaks observed at approximately 1,350 and 1,580 cm^{-1} are attributed to the characteristic D band of defects in carbon-based materials and the characteristic G band of vibrations of sp^2 hybridized carbon atoms[24,38]. Compared with pristine MXene, MXene@La-Ti-O exhibits a slight decrease in the G band, which may be ascribed from the increase of disordered carbon materials during the hydrothermal growth of La-Ti-O.

Figure 2E and Figure 2F show the N_2 (77 K) adsorption-desorption isotherms of MXene and MXene@La-Ti-O freestanding films, as well as the pore size distribution calculated by the Barrett−Joyner-Halenda method. As shown in Figure 2E, the pristine MXene film possesses a relatively small specific surface area of 36.714 m^2/g due to its densely stacked structure, while the MXene@La-Ti-O film exhibits a significantly larger specific surface area of 85.904 m^2/g and displays more micropores (approximately 2-40 nm). During the hydrothermal growth of La-Ti-O MOF, the organic linkers in the precursor can decompose to form porous carbon materials, and the *in-situ* growth of La-Ti-O MOF on MXene can act as a volume buffer and create many pores[39,40], which synergistically suppresses the restacking of MXene nanosheets, and increase the overall

porosity and specific surface area of the MXene@La-Ti-O film. Notably, the increase of porosity and specific surface area can not only provide more active sites for ion storage, but also facilitate more efficient ions accessibility and interaction between the electrolyte and electrode materials, thereby improving the electrochemical performance of the MXene@La-Ti-O film electrode[41,42].

Transmission electron microscopy (TEM) was used to investigate the morphology of MXene@La-Ti-O composite. Figure 3A shows that rod-shaped La-Ti-O MOFs are relatively uniformly loaded on MXene nanosheets. During the *in-situ* growth of La-Ti-O MOF on MXene, MXene can directly interact with the MOF precursor, and thus the interaction between MXene and La-Ti-O MOF is enough strong to show the clear TEM image of MXene@La-Ti-O composite. In addition, the strong interaction between MXene and La-Ti-O MOF is beneficial to improving the structural stability and electrochemical performance of MXene@La-Ti-O[43,44]. The corresponding EDS mapping of MXene@La-Ti-O is shown in Figure 3B, and the La elements are prominently highlighted at the locations of the rod-shaped MOF, demonstrating the successful integration of the MXene and La-Ti-O MOF. High-resolution TEM image of MXene@La-Ti-O [Figure 3C] reveals clear lattice fringes of MXene with a d-spacing of 0.37 nm, corresponding to the (004) crystal plane, which indicates the overall complete crystal structure of MXene in the MXene@La-Ti-O composite. Figure 3D shows the SEM image of MXene@La-Ti-O composite, and it is clearly observed that the La-Ti-O MOF nanorods are uniformly distributed on the surface of MXene nanosheets, further demonstrating the successful integration of the MXene and La-Ti-O MOF in the MXene@La-Ti-O composite. Figure 3E displays the cross-sectional SEM image of MXene@La-Ti-O freestanding film. Due to the *in-situ* growth of La-Ti-O MOF nanorods on MXene nanosheets, the MXene@La-Ti-O film shows relatively loose stacking with more pores and larger interlayer spacing compared to the pristine MXene film [Supplementary Figure 1], which is beneficial to facilitating electrolyte ions

transport and accessibility and thus improving the electrochemical performance of the MXene@La-Ti-O film electrode.

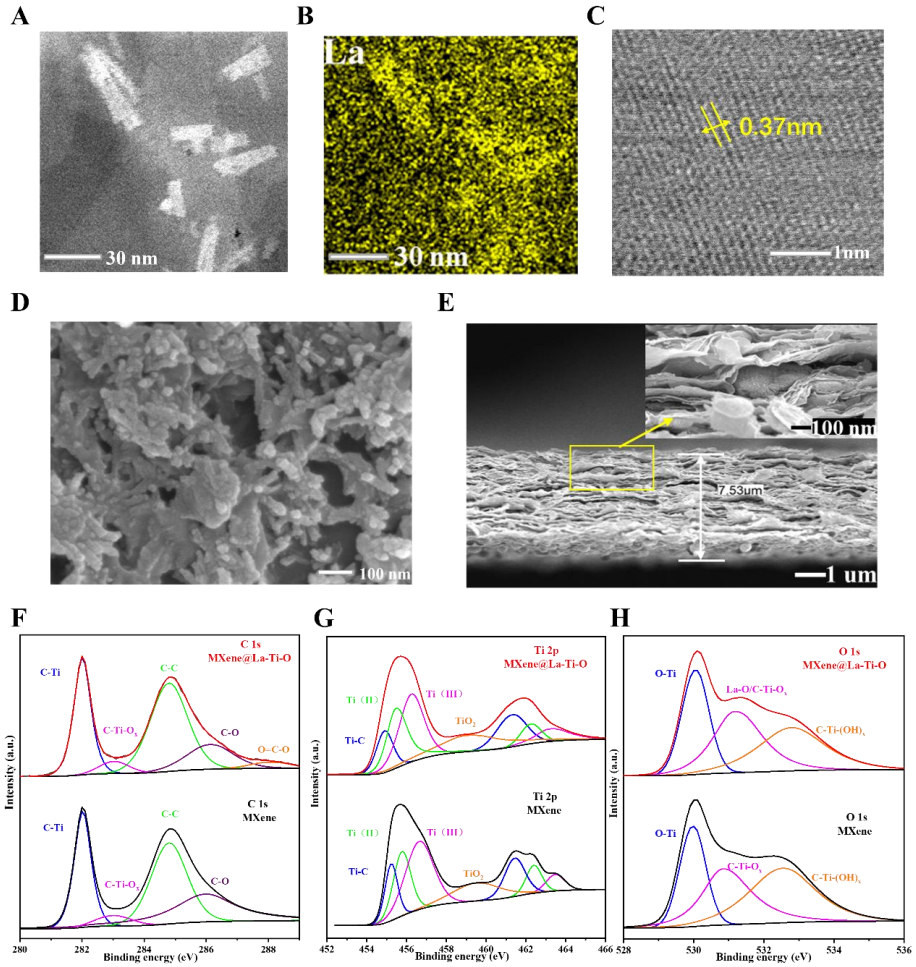

Figure 3. (A) TEM image and (B) corresponding La elemental EDS mapping of MXene@La-Ti-O; (C) High-resolution lattice fringe image of MXene@La-Ti-O; (D) Surface SEM image and (E) cross-sectional SEM image of MXene@La-Ti-O; The high-resolution (F) C 1s spectrum; (G) Ti 2p spectrum; and (H) O 1s spectrum for MXene and MXene@La-Ti-O.

X-ray photoelectron spectroscopy (XPS) was used to analyze the chemical composition of MXene@La-Ti-O. As shown in Supplementary Figure 2, the XPS survey spectrum of MXene@La-Ti-O shows extra La elements from La-Ti-O MOF compared to pristine MXene. The high-resolution C 1s, Ti 2p, and O 1s spectra of MXene@La-Ti-O and

MXene were further made comparison and analysis. The high-resolution C 1s spectrum [Figure 3F] displays four main types of bonds formed by C 1s: C−Ti, C−Ti−O_x, C−C, and C−O, located at approximately 282.2, 282.9, 284.8, and 286.5 eV, respectively[25,45]. According to the previous report[46], an additional O=C−O bond can be observed in MXene@La-Ti-O, which originates from the La-Ti-O MOF coordination. In C 1s spectrum, the relative content of C−Ti−O_x for MXene@La-Ti-O is increased to 6.27% than that (5.13%) of pristine MXene, which may result from the bonding between the surface positively charged Ti atoms of MXene and the negative electron oxygen atoms of La-Ti-O MOF. The high-resolution Ti 2p spectrum [Figure 3G] can be divided into three doublets located at approximately 454.8/460.8 eV, 456.0/462.1 eV, and 457.0/463.1 eV, as well as a single peak at around 458.7 eV, corresponding to Ti−C, Ti(II), Ti(III), and TiO_2 bonds, respectively[47]. The relative content of TiO_2 in MXene@La-Ti-O is decreased to 4.66% than that (5.31%) of pristine MXene, indicating that *in-situ* grown La-Ti-O MOF can reduce the oxidation of MXene and thus improve oxidation resistance of MXene@La-Ti-O. The high-resolution O 1s spectrum [Figure 3H] shows three distinct peaks at approximately 530.1, 531.5, and 533.2 eV, corresponding to O−Ti, La−O/C−Ti−O_x, and C−Ti−$(OH)_x$ bonds, respectively[25,48]. Since the binding energies of La−O and C−Ti−O_x both appear at around 531.5 eV and are difficult to distinguish, they are represented together. The La−O bond in MXene@La-Ti-O is attributed to the coordination structure within the La-Ti-O MOF. In O 1s spectrum, the relative content (20.45%) of La−O/C−Ti−O_x for MXene@La-Ti-O is obviously higher than that (18.61%) of pristine MXene, which may result from the contribution of La−O and the Ti−O bonding between the surface positively charged Ti atoms of MXene and the negative electron oxygen atoms of La-Ti-O MOF. Notably, the increase in the relative content of C−Ti−O_x can increase redox active sites, thereby enhancing the pseudocapacitance of MXene@La-Ti-O.

Oxidation resistance and mechanical property of MXene@La-Ti-O film

The stability of MXene-based electrode materials is also critical for commercial application. The oxidation resistance of MXene@La-Ti-O were further investigated by adding a small amount of strong oxidizing agent (hydrogen peroxide, H_2O_2) into the MXene@La-Ti-O dispersion. Figure 4A shows optical images of MXene and MXene@La-Ti-O dispersions before and after the introduction of an equal amount of H_2O_2, where (1) and (2) represent the MXene and MXene@La-Ti-O dispersions, respectively. Initially, both MXene and MXene@La-Ti-O dispersions appear as uniformly dispersed black colloidal solutions. After 12 h of adding H_2O_2, most of MXene dispersion turns yellow due to the severe oxidation, while the MXene@La-Ti-O dispersion is almost unchanged, showing significantly improved oxidation resistance. The *in-situ* growth of La-Ti-O MOF on MXene facilitates the strong interaction between La-Ti-O MOF and MXene, effectively inhibiting the oxidation of MXene and maintaining its structural integrity, and thus enabling the significantly improved oxidation resistance of MXene@La-Ti-O[39,49].

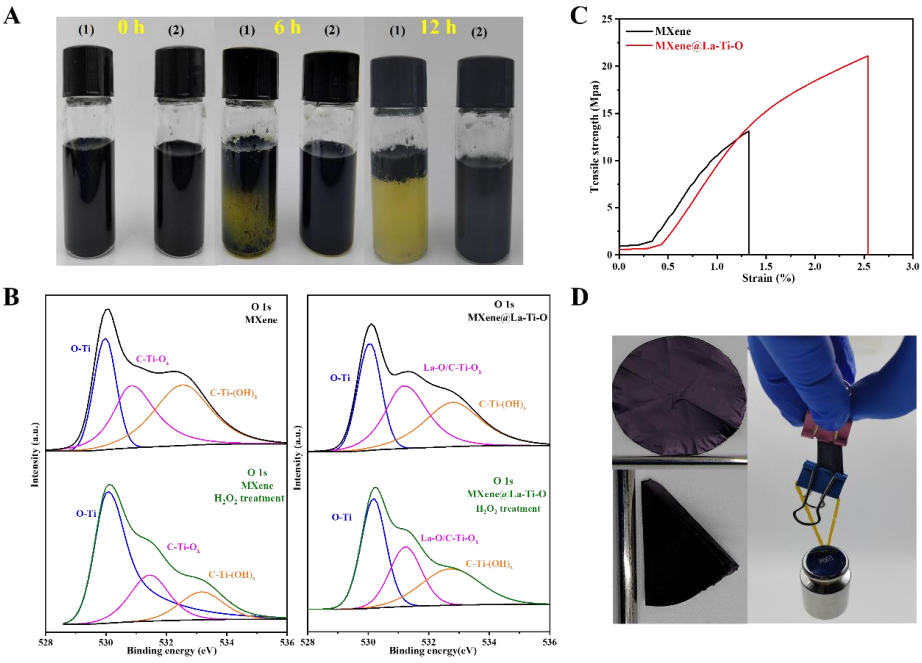

Figure 4. (A) Digital photos of the oxidation process of MXene (1) and MXene@La-Ti-O (2) at 0 h, 6 h, and 12 h from left to right; (B) Comparison of high-resolution O 1s XPS spectra of MXene and MXene@La-Ti-O before and after

oxidation treatment; (C) Tensile strain curves of MXene film and MXene@La-Ti-O film; (D) Folding and unfolding images of the free-standing MXene@La-Ti-O film and its load-bearing with weights.

In order to further analyze the antioxidant mechanism, XPS measurement was performed on MXene@La-Ti-O and MXene samples oxidized with H_2O_2 for 12 h. Figure 4B and Supplementary Figure 3 separately display the high-resolution O 1s and Ti 2p XPS comparison of samples before and after oxidation, and the relevant data is summarized in Supplementary Table 1. In O 1s spectra of MXene, the relative content of C−Ti−$(OH)_x$ and C−Ti−O_x are both obviously decreased and the relative content of O−Ti is obviously increased after H_2O_2 oxidation, indicating the severe oxidation of MXene by H_2O_2. In Ti 2p spectra of MXene, the relative content of TiO_2 is also obviously increased by 61% (from 5.31% to 8.53%) after H_2O_2 oxidation, further demonstrating the severe oxidation of MXene by H_2O_2. However, for MXene@La-Ti-O, the relative content changes of C−Ti−$(OH)_x$ and C−Ti−O_x and O−Ti in O 1s spectra before and after H_2O_2 oxidation are all significantly smaller, and the relative content of TiO_2 in Ti 2p spectra is only slightly increased by 30% (from 4.66% to 6.07%) after H_2O_2 oxidation, demonstrating the significantly improved oxidation resistance of MXene@La-Ti-O.

The mechanical strength of freestanding film electrode is also important for practical application. The mechanical properties of the freestanding films were evaluated through strain-stress testing, as shown in Figure 4C. Compared with pristine MXene film, the strain of the MXene@La-Ti-O film is increased from 1.326% to 2.539%, and the tensile stress is increased from 13.18 MPa to 21.10 MPa, indicating a notable enhancement in the toughness of the MXene@La-Ti-O film due to the strong interaction between La-Ti-O MOF and MXene. Figure 4d shows a simple folding and recovery test of the MXene@La-Ti-O film. After folding and restoration, the MXene@La-Ti-O film did not

rupture and was still able to lift up to 100 grams of weight without tearing, demonstrating excellent mechanical strength and flexibility, which corresponds to the significantly enhanced toughness observed in Figure 4C.

Electrochemical performance of MXene@La-Ti-O film electrode

The electrochemical performance of MXene@La-Ti-O film as supercapacitor electrode was measured by using a three-electrode system based on a 3M H_2SO_4 electrolyte. First, the weight content of La-Ti-O MOF in MXene@La-Ti-O composite was optimized, and the electrochemical performances of MXene@La-Ti-O film electrode with different weight content of La-Ti-O MOF are shown in Supplementary Figure 4. The comparative results of cyclic voltammetry (CV) and galvanostatic charge-discharge (GCD) curves for MXene@La-Ti-O film electrode suggest that the MXene@La-Ti-O film electrode with 23% weight content of La-Ti-O MOF achieves the best electrochemical performance. Therefore, the electrochemical performance of the optimal MXene@La-Ti-O film electrode was further investigated by comparison with the pristine MXene film electrode.

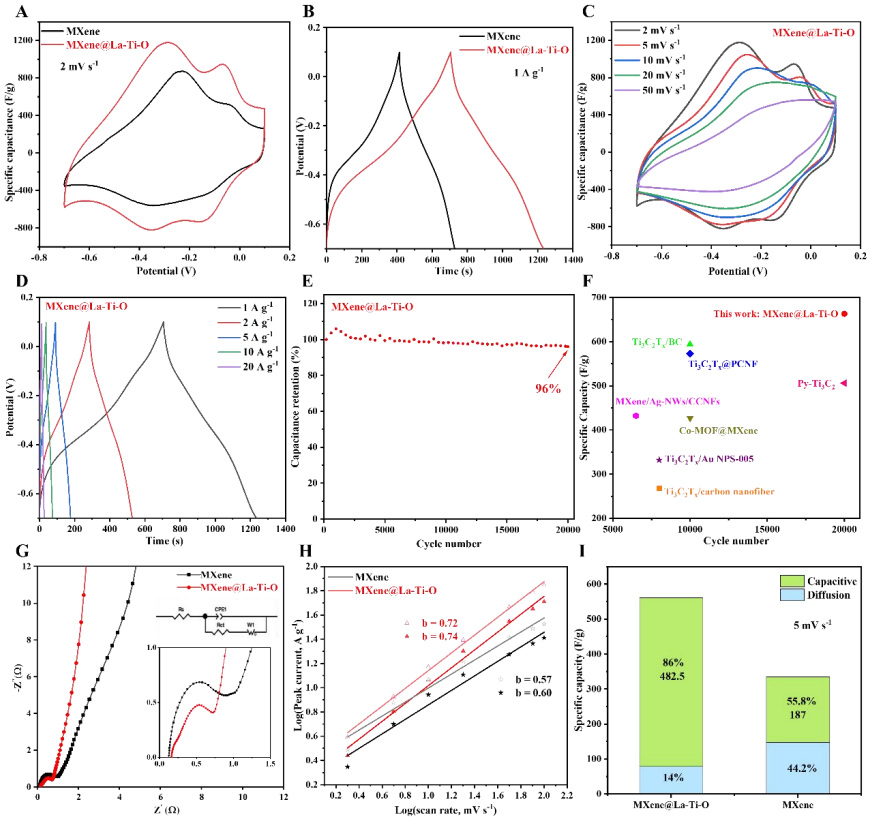

Figure 5. (A) CV and GCD curves of $Ti_3C_2T_x$ and MXene@La-Ti-O film electrodes at 2 mV s^{-1} and (B) 1 A g^{-1}; (C) CV curves of MXene@La-Ti-O film electrode at different scan rates; (D) specific capacitance of MXene@La-Ti-O film electrode at different scan rates; (E) comparison Chart of Capacitance Contribution Rates between MXene and MXene@La-Ti-O; (F) electrochemical impedance spectroscopy; (G) cycling stability curve of MXene@La-Ti-O film electrode at 10 A g^{-1}; (H) kinetic b-value analysis; (I) performance comparison of different film electrodes.

Figure 5A shows the CV curves of MXene@La-Ti-O and MXene film electrodes at a scan rate of 2 mV s^{-1}. Compared with the MXene film electrode, the MXene@La-Ti-O film electrode displays a larger integrated CV area and higher current response within the potential window of −0.7 to 0.1 V, achieving a significantly larger capacitance of 615 F·g^{-1}. Figure 5B shows the GCD curves of MXene@La-Ti-O and MXene film electrodes at a current density of 1 A g^{-1}. Compared with MXene, the MXene@La-Ti-O film electrode exhibits a significantly longer charge-discharge time and a more symmetrical GCD curve, and demonstrates a notably higher capacitance of 663 F·g^{-1},

indicating a 63.4% increase over MXene. The CV curves at different scan rates and GCD curves at different current densities of MXene@La-Ti-O film electrode are shown in Figure 5C and Figure 5D, respectively, and the calculated specific capacitances are summarized in Supplementary Figure 5. The specific capacitances of the MXene@La-Ti-O film electrode slowly decrease from 615 F g^{-1} at 2 mV s^{-1} to 267 F g^{-1} at 50 mV s^{-1} and from 663 F g^{-1} at 1 A g^{-1} to 325 F g^{-1} at 20 A g^{-1}, indicating that the MXene@La-Ti-O film electrode possesses good rate performance. In addition, the MXene@La-Ti-O film electrode exhibits high capacitance retention of 96% after 20,000 cycles at 20 A g^{-1} [Figure 5E], indicating excellent cycling stability. Figure 5F displays the specific capacitances comparison of this work to other MXene-based film electrodes reported in recent years, and Supplementary Table 2 summarizes the detailed conditions and parameters. Apparently, the excellent electrochemical performance (high capacitance of 663 F g^{-1} at 1 A g^{-1} and high stability of 96% retention after 20,000 cycles) of the MXene@La-Ti-O film electrode outperforms most of MXene-based film electrodes reported so far.

The electrochemical impedance spectroscopy (EIS) Nyquist plots of film electrodes and the equivalent circuit diagram fitted using Zview software are shown in Figure 5G. The series resistance (R_s) and charge transfer resistance (R_{ct}) of MXene film electrode are calculated to be 0.80 and 0.60 Ω, respectively. However, the MXene@La-Ti-O film electrode shows obviously lower R_s 0.59 Ω and smaller R_{ct} of 0.32 Ω, indicating more efficient ions transport and charge transfer. The *in-situ* grown La-Ti-O MOF effectively weakens the re-stacking of MXene nanosheets and significantly increases the interlayer spacing, thus enabling the improved ions transport and charge transfer in the MXene@La-Ti-O film electrode. The charge storage kinetics was further analyzed by investigating the correlation between peak current and scan rate with the equation of $i_P=av^b$, where i_p and v separately represents the peak current and scan rate, and a and b are parameters. As shown in Figure 5H, the MXene film electrode possesses the b

values of 0.60 and 0.57 under cathodic and anodic sweep, respectively. However, the MXene@La-Ti-O film electrode shows obviously larger *b* values of 0.74 and 0.72 under cathodic and anodic sweep, respectively, indicating significantly improved kinetic properties. The capacitive-/diffusion-controlled charge storage processes were also analyzed by using the equation of $i(V)=k_1v+k_2v^{1/2}$, where $i(V)$ represents the current at a fixed potential, including the capacitive process (k_1v) and diffusion-controlled process ($k_2v^{1/2}$). As shown in Figure 5I, the MXene@La-Ti-O film electrode shows a significantly higher capacitive contribution of 86% compared to the MXene film electrode with a capacitive contribution of 55.8% at 5 mV s^{-1}, which is attributed to the improved ions transport and charge transfer in the MXene@La-Ti-O film electrode.

Flexible solid-state supercapacitor devices

A flexible solid-state symmetric supercapacitor [Figure 6A] was fabricated by sandwiching a PVA/H_2SO_4 gel electrolyte between two symmetric film electrodes. The GCD curves at 0.5 A g^{-1} of MXene-based control device and MXene@La-Ti-O-based device are displayed in Figure 6A. The MXene@La-Ti-O device shows an obviously larger specific capacitance of 113.3 F g^{-1} compared to the MXene device (64.2 F g^{-1}). Figure 6B and Figure 6C separately display the CV curves at different scan rates and GCD curves at different current densities of the MXene@La-Ti-O device, indicating high rate performance. Moreover, the energy storage performance of MXene@La-Ti-O device can be calculated based on the GCD results, and the MXene@La-Ti-O device achieves a high energy density of 58.93 Wh kg^{-1} at a high power density of 400 W kg^{-1}. Figure 6D shows the capacitance retention of MXene@La-Ti-O device after different charge-discharge cycles. The MXene@La-Ti-O device still possesses a high capacitance retention of 84% after 5000 cycles at 10 A g^{-1}, indicating excellent cycling stability. Figure 6E displays the energy storage performance comparison of this work to other MXene-based flexible supercapacitor devices reported in recent years, and Supplementary Table 3 summarizes the detailed conditions and parameters. Apparently,

the energy storage performance of MXene@La-Ti-O device outperforms most of MXene-based flexible sandwiched supercapacitor devices reported so far. Figure 6f displays the electrochemical performance of flexible MXene@La-Ti-O devices under bending condition and the digital photo of illuminated LEDs lit by three devices connected in series under different bending conditions. The MXene@La-Ti-O devices show similar GCD curves under bending angles of 0°, 45°, and 90°, and the brightness of the LEDs remains almost unchanged under bending condition, indicating high bending stability. Moreover, the high bending stability would provide great application potential of MXene@La-Ti-O film electrode in flexible energy storage devices.

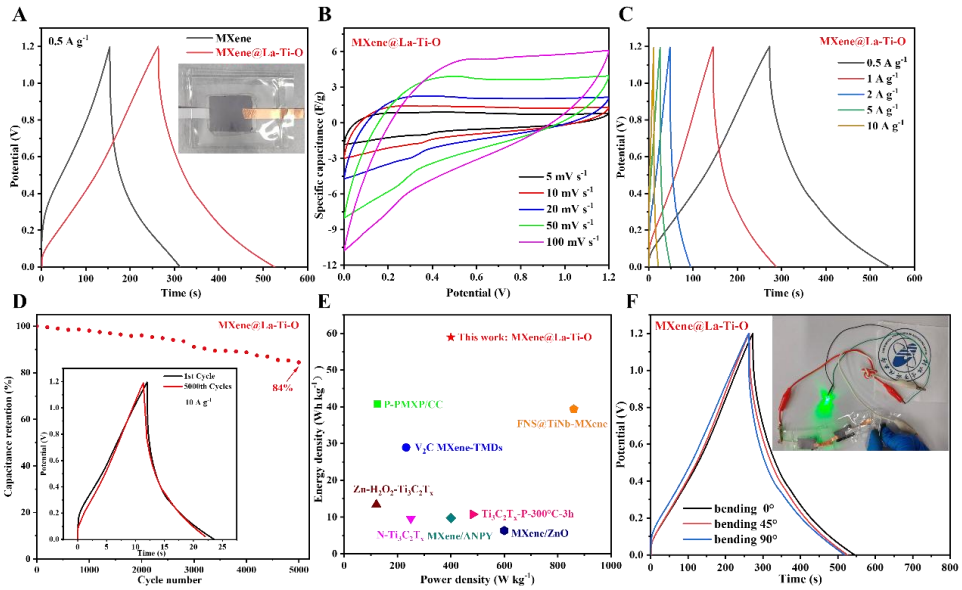

Figure 6. (A) Cyclic voltammetry curves at different scan rates of the PVA/H_2SO_4-type sandwich device MXene@La-Ti-O; (B) charge-discharge curves; (C) CV curves of MXene@La-Ti-O and $Ti_3C_2T_x$ devices at 5 mV s^{-1}; (D) GCD curves at 0.5 A g^{-1}; (E) stability test of the MXene@La-Ti-O device at 10 A g^{-1}; (F) photograph of the MXene@La-Ti-O device.

CONCLUSIONS

In conclusion, La-Ti-O MOF is *in-situ* grown from lanthanum-coordinated titanium-oxo cluster precursors on $Ti_3C_2T_x$ MXene nanosheets to construct the MXene@La-Ti-O

composite. The *in-situ* grown La-Ti-O MOF effectively inhibits the restacking of MXene nanosheets and modulates the pore structure of the composite, thereby optimizing the ion diffusion pathways and increasing the redox active sites. Simultaneously, the structural coupling of MXene@La-Ti-O improves the oxidation resistance and mechanical toughness of free-standing film. The MXene@La-Ti-O film electrode shows excellent electrochemical performance with high capacitance of 663 F g^{-1} at 1 A g^{-1} and high stability of 96% retention after 20,000 cycles. Moreover, the MXene@La-Ti-O symmetric supercapacitor exhibits superior energy storage performance with energy density of 58.93 Wh kg^{-1} at power density of 400 W kg^{-1}, which is among the best performances reported so far for MXene-based flexible symmetric solid-state supercapacitors. The impressive results indicate the synergistic structural coupling strategy of MXene and La-Ti-O MOF is very promising for high-performance flexible supercapacitors.

DECLARATIONS

Authors' contributions

Data curation, formal analysis, methodology, writing - original draft: H.H;

Conceptualization, funding acquisition, supervision, writing-review and editing: C.P;

Data curation: L.X, X.Y;

Visualization: D.Y, Z.K;

Writing-review and editing: W.S;

Conceptualization: Z.H.;

Methodology: X.F;

Funding acquisition, writing-review and editing: S.L.

Availability of data and materials

Some results of supporting the study are presented in the Supplementary Materials. Other raw data that support the findings of this study are available from the

corresponding author upon reasonable request.

Financial support and sponsorship

This work was supported by the Natural Science Foundation of Guangxi Province (2024GXNSFAA010090), Guangxi Bagui Young Top Talent Foundation, National Natural Science Foundation of China (Nos. 52371218, 52461032, 52271205, 552101245), Guangxi S&T Program (AA24206022, 2021AB17045, AB21220027), National Key Research and Development Program of China (2022YFB4003200), Guilin Lijiang Scholar Foundation, and Guangxi Key Laboratory of Information Materials (Guangxi Science and Technology Program AD25069070).

Conflict of interest

All authors declared that there are no conflicts of interest.

Ethical approval and consent to participate

Not applicable.

Consent for publication

Not applicable.

REFERENCES

1. Inman, A.; Hryhorchuk, T.; Bi, L.; et al. Wearable energy storage with MXen e textile supercapacitors for real world use. *J.Mater.Chem.A.* **2023**, *11* (7), 3514-2 3, [DOI: 10.1039/D2TA08995E]

2. Shalini, S.; Naveen, T.B.; Durgalakshmi, D.; et al. Progress in flexible superca pacitors for wearable electronics using graphene-based organic frameworks. *J.Ener gy Storage* **2024**, *86*, 111260.[DOI: 10.1016/j.est.2024.111260]

3. Liu, B.; Ye, Y.; Yang, M.; et al. All-in-one Biomass-Based Flexible Supercapa citors with High Rate Performance and High Energy Density. *Adv.Funct.Materials.* **2024**, *34* (10), 2310534.[DOI: 10.1002/adfm.202310534]

4. Mehmood, A.; Ijaz, I.; Raza, W.; et al. Toward flexible energy storage: MXen e frameworks from synthesis principles to device applications. *Prog.Mater.Sci.* **20 26**, *156*, 101583.[DOI: 10.1016/j.pmatsci.2025.101583]

5. Xue, Q.; Sun, J.; Huang, Y.; et al. Recent Progress on Flexible and Wearable Supercapacitors. *Small* **2017**, *13* (45), 1701827.[DOI: 10.1002/smll.201701827]

6. Cao, Y.; Sun, S.; Li, W.; et al. Challenge and technological trends of flexible solid-state supercapacitors. *J.Energy Storage* **2024**, *97*, 112837.[DOI: 10.1016/j.es t.2024.112837]

7. Liu, J.; Xia, Q.; Wang, L.; et al. In Situ Growth of Nanorod-Shaped Ni,Co-M OF on Mo2CTx MXene Surface to Realize Enhanced Energy Storage for Superc apacitors. *ACS.Appl.Mater.Interfaces* **2024**, *16* (37), 49380-91.[DOI: 10.1021/acsam i.4c09616]

8. Wu, Y.; Li, Y. MXene/Cellulose Composites Enabling Next-Generation Sports Smart Wearables: Progress, Challenges, and Prospects. *ACS.Appl.Mater.Interfaces* **2026**, *18* (17), 23989-4008.[DOI: 10.1021/acsami.6c04619]

9. M, M.; P, S.A.; Pachamuthu, S.; et al. Synthesis of a MXene/Metal-Organic F ramework Composite for Efficient Supercapacitor and Electrocatalytic CO2 Reduc tion. *ACS.Appl.Mater.Interfaces* **2025**, *17* (37), 51996-2009.[DOI: 10.1021/acsami.5 c07809]

10. Payam, A.F.; Khalil, S.; Chakrabarti, S. Synthesis and Characterization of M OF-Derived Structures: Recent Advances and Future Perspectives. *Small* **2024**, *20* (32), 2310348.[DOI: 10.1002/smll.202310348]

11. Zheng, C.; Jiang, P.; Rui, C.; et al. Graphene and MXene fibers: rising stars for emerging smart textiles. *Soft Sci.* **2026**, *6* (2), 32.[DOI: 10.20517/ss.2025.157]

12. Meng, X.; Zhou, W.; Lin, N.; et al. Inducing multiple polarizations in core@double-shell structured MXene/PVDF flexible nanodielectrics toward elevated over all dielectric performances. *Soft Sci.* **2025**, *5* (4), 59.[DOI: 10.20517/ss.2025.65]

13. Xu, T.; He, Q.; Chen, H.; et al. Principle and Structural Design of MXene-Based Sensors Toward Smart Life. *Interdiscip.Mater.* **2025**, *4* (2), 284-99.[DOI: 10.1002/idm2.12238]

14. Yang, W.; Liu, F.; Lin, Y.; et al. MXene-based flexible sensors for wearable applications. *Soft Sci.* **2025**, *5* (3), 33.[DOI: 10.20517/ss.2025.12]

15. Safari, M.; Mazloom, J. Outstanding energy storage performance in CoFe bimetallic metal-organic framework spindles via decorating with reduced graphene oxide nanosheets. *J.Energy Storage* **2023**, *58*, 106390.[DOI: 10.1016/j.est.2022.106390]

16. Zheng, K.; Liao, L.; Zhang, Y.; et al. Hierarchical NiCo-LDH core/shell hom ostructural electrodes with MOF-derived shell for electrochemical energy storage. *J.Colloid Interface Sci.* **2022**, *619*, 75-83.[DOI: 10.1016/j.jcis.2022.03.056]

17. Yin, X.; Alsuwaidi, A.; Zhang, X. Hierarchical metal-organic framework (MOF) pore engineering. *Micropor.Mesopor.Mater.* **2022**, *330*, 111633.[DOI: 10.1016/j.micromeso.2021.111633]

18. Chafiq, M.; Chaouiki, A.; Ryu, J.; et al. Beyond conventional: Role of chiral metal-organic frameworks in asymmetric scenarios. *Nano Today* **2024**, *56*, 102227.[DOI: 10.1016/j.nantod.2024.102227]

19. Zhao, L.-L.; Wang, J.-Y.; Wu, Y.-M.; et al. Unlocking the multidimensional application and optimization mechanism of MOFs materials in aqueous zinc ion batteries. *J.Energy Chem.* **2025**, *111*, 249-73.[DOI: 10.1016/j.jechem.2025.07.063]

20. Cui, Y.; Zhao, L.; He, D.; et al. Preparation of Zirconium-Based MOF-Derived Phosphide on GO/MXene Double Substrates for High-Performance Asymmetric Supercapacitors. *ACS.Appl.Mater.Interfaces* **2024**, *16* (36), 47751-62.[DOI: 10.1021/acsami.4c10803]

21. Gao, M.; Wang, F.; Yang, S.; et al. Engineered 2D MXene-based materials for advanced supercapacitors and micro-supercapacitors. *Mater.Today* **2024**, *72*, 318-358.[DOI: 10.1016/j.mattod.2023.12.009]

22. Zhao, Z.; Xu, Z.; Wang, Y.; et al. Scalable assembly of flexible ultrathin all-in-one MXene-based supercapacitors. *J.Mater.Chem.A.* **2025**, *13* (18), 13175-13185, [DOI: 10.1039/D5TA00327J.10.1039/D5TA00327J]

23. Cao, W.; Gong, P.; Wang, W.; et al. A Highly Stable MXene Aqueous Conductive Ink for Inkjet Printing Flexible Microsupercapacitors. *ACS.Appl.Mater.Interfaces* **2026**, *18* (17), 24728-41.[DOI: 10.1021/acsami.6c03460]

24. Lai, M.; Chen, K.; Wang, D.; et al. Protective hydrothermal treatment to improve ion pathway in Ti3C2Tx MXene for high-performance flexible supercapacitors. *Mater.Today Nano* **2024**, *25*, 100450.[DOI: 10.1016/j.mtnano.2023.100450]

25. Lai, M.; Zhao, C.; Wang, D.; et al. Significantly Enhanced Oxidation Resistance and Electrochemical Performance of Hydrothermal Ti3C2Tx MXene and Tannic Acid Composite for High-Performance Flexible Supercapacitors. *ACS.Appl.Mater.Interfaces* **2024**, *16* (41), 55555-68.[DOI: 10.1021/acsami.4c13838]

26. Zou, H.; He, B.; Kuang, P.; et al. Metal-Organic Framework-Derived Nickel-Cobalt Sulfide on Ultrathin Mxene Nanosheets for Electrocatalytic Oxygen Evolution. *ACS.Appl.Mater.Interfaces* **2018**, *10* (26), 22311-9.[DOI: 10.1021/acsami.8b06272]

27. Wu, H.; Almalki, M.; Xu, X.; et al. MXene Derived Metal-Organic Frameworks. *J.Am.Chem.Soc.* **2019**, *141* (51), 20037-42.[DOI: 10.1021/jacs.9b11446]

28. Tan, Y.; Yang, L.; Zhai, D.; et al. MXene-Derived Metal-Organic Framework @MXene Heterostructures toward Electrochemical NO Sensing. *Small* **2022**, *18* (50), 2204942.[DOI: 10.1002/smll.202204942]

29. Zheng, S.; Zhou, H.; Xue, H.; et al. Pillared-layer Ni-MOF nanosheets ancho red on Ti3C2 MXene for enhanced electrochemical energy storage. *J.Colloid Inte rface Sci.* **2022**, *614*, 130-7.[DOI: 10.1016/j.jcis.2022.01.094]

30. Shah, S.S.; Aziz, M.A.; Rasool, P.I.; et al. Electrochemical synergy and futur e prospects: Advancements and challenges in MXene and MOFs composites for hybrid supercapacitors. *Sustain.Mater.Technol.* **2024**, *39*, e00814.[DOI: 10.1016/j.su smat.2023.e00814]

31. Issah, I.; Noor, M.M.; Kadirgama, K.; et al. Elucidating the synergy of MXe ne and Metal-Organic framework composite for superior electrochemical energy st orage applications. *Prog.Mater.Sci.* **2026**, *158*, 101635.[DOI: 10.1016/j.pmatsci.202 5.101635]

32. Xie, Y.-L.; Fang, W.-H.; Zhang, J. Aggregation of titanium-oxo clusters. *Aggr egate* **2024**, *5* (3), e506.[DOI: 10.1002/agt2.506]

33. Zhang, L.; Fan, X.; Yi, X.; et al. Coordination-Delayed-Hydrolysis Method fo r the Synthesis and Structural Modulation of Titanium-Oxo Clusters. *Acc.Chem.Re s.* **2022**, *55* (21), 3150-61.[DOI: 10.1021/acs.accounts.2c00421]

34. Li, N.; Yang, P.; Pan, M.-Y.; et al. Lanthanide–containing titanium-oxo cluste rs with high aqueous stability for photocatalytic application. *J.Mol.Struct.* **2022**, *1 263*, 133169.[DOI: 10.1016/j.molstruc.2022.133169]

35. Romero-Muñiz, I.; Romero-Muñiz, C.; del Castillo-Velilla, I.; et al. Revisiting Vibrational Spectroscopy to Tackle the Chemistry of Zr6O8 Metal-Organic Fram ework Nodes. *ACS.Appl.Mater.Interfaces* **2022**, *14* (23), 27040-7.[DOI: 10.1021/ac sami.2c04712]

36. Wang, K.; Feng, S.; Ma, P. Synthesis, characterization and photoluminescence properties of a benzoic modified lanthanide-containing polyoxometalate. *Inorg.Chem.Commun.* **2019**, *108*, 107511.[DOI: 10.1016/j.inoche.2019.107511]

37. Ma, R.; Zhang, X.; Zhuo, J.; et al. Self-Supporting, Binder-Free, and Flexible Ti3C2Tx MXene-Based Supercapacitor Electrode with Improved Electrochemical Performance. *ACS Nano* **2022**, *16* (6), 9713-27.[DOI: 10.1021/acsnano.2c03351]

38. Yu, J.; Zeng, M.; Zhou, J.; et al. A one-pot synthesis of nitrogen doped porous MXene/TiO2 heterogeneous film for high-performance flexible energy storage. *Chem.Eng.J.* **2021**, *426*, 130765.[DOI: 10.1016/j.cej.2021.130765]

39. Chaouiki, A.; Chafiq, M.; Salghi, R.; et al. Versatile integration of MOF and MXene composites for next-generation hybrid energy storage solutions. *J.Energy Chem.* **2025**, *104*, 687-715.[DOI: 10.1016/j.jechem.2025.01.012]

40. Ye, Z.; Jiang, Y.; Li, L.; et al. Self-Assembly of 0D-2D Heterostructure Electrocatalyst from MOF and MXene for Boosted Lithium Polysulfide Conversion Reaction. *Adv.Mater.* **2021**, *33* (33), 2101204.[DOI: 10.1002/adma.202101204]

41. Cao, P.; Liu, Y.-L.; Zhang, Q.; et al. MXene/MOF composites: Synergistic platforms for advanced Energy, catalysis, and environmental applications. *Coord.Chem.Rev.* **2025**, *545*, 217018.[DOI: 10.1016/j.ccr.2025.217018]

42. Venkateswarlu, S.; Vallem, S.; Umer, M.; et al. Recent progress on MOF/MXene nanoarchitectures: A new era in coordination chemistry for energy storage and conversion. *J.Energy Chem.* **2023**, *86*, 409-36.[DOI: 10.1016/j.jechem.2023.07.044]

43. Ji, Y.; Li, W.; You, Y.; et al. In situ synthesis of M (Fe, Cu, Co and Ni)-MOF@MXene composites for enhanced specific capacitance and cyclic stability in supercapacitor electrodes. *Chem.Eng.J.* **2024**, *496*, 154009.[DOI: 10.1016/j.cej.2024.154009]

44. Chen, X.; Xia, S.; Tan, T.; et al. In situ growth of MOF-derived nitrogen-doped carbon nanotubes on hollow MXene spheres for K-ion storage. *Inorg.Chem.Front.* **2023**, *10* (15), 4414-24, [DOI: 10.1039/D3QI00763D.10.1039/D3QI00763D]

45. Wang, Y.; Chen, N.; Liu, Y.; et al. MXene/Graphdiyne nanotube composite films for Free-Standing and flexible Solid-State supercapacitor. *Chem.Eng.J.* **2022**, *450*, 138398.[DOI: 10.1016/j.cej.2022.138398]

46. Wang, C.; Zhang, J.; Zhu, X. Synthesis of lanthanide-doped titanium-oxo clusters for efficient photocurrent responses. *J.Solid State Chem.* **2021**, *304*, 122586. [DOI: 10.1016/j.jssc.2021.122586]

47. Natu, V.; Benchakar, M.; Canaff, C.; et al. A critical analysis of the X-ray photoelectron spectra of Ti3C2Tz MXenes. *Matter* **2021**, *4* (4), 1224-51.[DOI: 10.1016/j.matt.2021.01.015]

48. Yoo, H.J.; Yoon, S.Y.; Wong, K.T.; et al. Enhanced fluoride adsorption via coordination tuning in metal-organic frameworks. *Chem.Eng.J.* **2025**, *507*, 160451. [DOI: 10.1016/j.cej.2025.160451]

49. Nam, S.; Mahato, M.; Matthews, K.; et al. Bimetal Organic Framework-Ti3C2Tx MXene with Metalloporphyrin Electrocatalyst for Lithium-Oxygen Batteries. *Adv.Funct.Materials.* **2023**, *33* (1), 2210702.[DOI: 10.1002/adfm.202210702]